*Rev. Roum. Sci. Techn.– Électrotechn. et Énerg.*
Vol. **69**, *2*, pp. 177–182, Bucarest, 2024

# THREE-LEVEL DIRECT TORQUE CONTROL BASED ON COMMON MODE VOLTAGE REDUCTION STRATEGY FED TWO PARALLEL CONNECTED FIVE-PHASE INDUCTION MACHINE

KHALED MOHAMMED SAID BENZAOUI [1], ELAKHDAR BENYOUSSEF [1], AHMED ZOUHIR KOUACHE[1]

**Keywords: Common mode voltage (CMV); Direct torque control (DTC); Parallel connected drive; Five-phase induction machine (FPIM); Five-phase three-level inverter.**

**This survey proposes a mitigation approach for common mode voltage produced in a three-level five-phase inverter fed two parallel-connected five-phase induction machines controlled by direct torque control. The switching frequencies used in the inverter fed these types of drives are characterized by a large amplitude of the produced common mode voltage waveforms ($\pm V_{dc}/2$), leading to prominent issues, especially with the near introduction of wide-gap semiconductor technologies. In this context, the introduced approach is an extension to a multi-motor drive of the TATTE method, exploiting the concept of virtual voltage vectors to mitigate the resulting common mode voltage. The collected results critically evaluate the reported approach by improving the drive's generated common mode voltage status to ($\pm V_{dc}/10$) compared to ($\pm V_{dc}/2$) in the conventional method, in addition to a significant reduction in the flux and torque ripples by 22 % and 39 %, respectively, at the cost of an insignificant increase in the current harmonic content by 6 %.**

## 1. INTRODUCTION

In most industrial processes, three-phase induction machines are the primary electromechanical actuators, such as lifts [1] and air conditioning [2], etc. Since modern drives, because of the intermediate dc link, became independent from the nature of the power source, the tendency for multiphase machine solutions has been increasing perpetually due to their characteristic features reported in [3,4]. The five-phase induction machines (FPIM) are candidates that offer a fair balance between the overall system advantages and complexity [5].

From the point of view of the FPIM control, several strategies have been developed to improve their performance [6] in the field of adjustable speed drives. It is now extensively investigated for its superiority in faster and more precise control and response over mechanical variables. Further performance improvement has been introduced and reported in [7–10].

Despite the advantages of the voltage source inverter, the CMV waveforms are the natural result of the PWM-controlled drives working under several kHz of switching frequency. In conjunction with the parasitic capacitances, this phenomenon results in the flow of common mode currents through different parts of the machine to the ground, inducing severe drawbacks such as bearing aging, winding insulation failure, unanticipated tripping of the ground current protection, and EMI [11–14].

Within this framework, the scientific society makes various contributions to reduce the impact of the common mode voltage (CMV) through preventive or corrective measures [11–13]. It reports the current state of the art in this field.

Thus, the primary purpose of the present work is to study an extension of a mitigation technique of CMV reported in [15] for two parallel connected FPIM drive ($DTC_{CMV}$) fed by a three-level five-phase inverter (THL-FP), taking into consideration the existing degree of freedom (DOF) in multiphase power converters.

The structure of this manuscript is as follows: section 2 describes the mathematical model of the two-motor drive, and section 3 states the basics of $DTC_c$. Section 4 gives the two control schemes' CMV status and theoretical waveforms. Section 5 states the extension of TATTE method to a multi-machine drive. The effectiveness of the proposed method is evaluated through the simulation results in section 6. In the last section, a conclusion is made.

## 2. TWO FPIMs MODELING

Figure 1 depicts a THL-FP inverter feeding two parallel-connected squirrel cage FPIMs five with distributed stator windings spatially shifted by 72 electrical degrees star connected, omitting the zero-sequence current component. [16] reports the mathematical model of the considered THL-FP inverter.

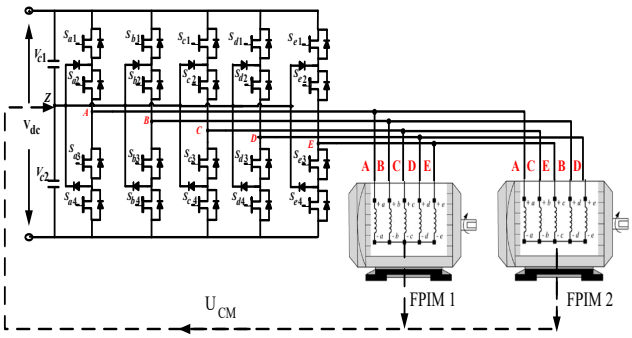


Fig. 1 – Schematic illustration of THL-FP inverter fed two FPIM connected in parallel.

In this topology, the $\alpha\beta_1$ plane and $\alpha\beta_2$ plane are exceeded by the application of Clark's transformation to the output of the phase-to-neutral voltages [16]:

$$[C]=\frac{2}{5}\begin{bmatrix} 1 & \cos\left(\frac{2\pi}{5}\right) & \cos\left(\frac{4\pi}{5}\right) & \cos\left(\frac{6\pi}{5}\right) & \cos\left(\frac{8\pi}{5}\right) \\ 0 & \sin\left(\frac{2\pi}{5}\right) & \sin\left(\frac{2\pi}{5}\right) & \sin\left(\frac{2\pi}{5}\right) & \sin\left(\frac{2\pi}{5}\right) \\ 1 & \cos\left(\frac{6\pi}{5}\right) & \cos\left(\frac{8\pi}{5}\right) & \cos\left(\frac{2\pi}{5}\right) & \cos\left(\frac{4\pi}{5}\right) \\ 0 & \sin\left(\frac{6\pi}{5}\right) & \sin\left(\frac{8\pi}{5}\right) & \sin\left(\frac{2\pi}{5}\right) & \sin\left(\frac{4\pi}{5}\right) \\ \frac{1}{2} & \frac{1}{2} & \frac{1}{2} & \frac{1}{2} & \frac{1}{2} \end{bmatrix} \quad (1)$$

The relationships between the inverter voltages and currents components and the two machine terminals are given:

[1] University of Kasdi Merbah, Faculty of Science Applied, Department of Electrical Engineering, Laboratoire LAGE, Ouargla 30000, Algeria. E-mails: benzaoui.khaled@univ-ouargla.dz, benyoussef.elakhdar@univ-ouargla.dz, Kouache.ahmed@univ-ouagla.dz

DOI: 10.59277/RRST-EE.2024.69.2.10

$$\begin{bmatrix} V_A^{inv} \\ V_B^{inv} \\ V_C^{inv} \\ V_D^{inv} \\ V_E^{inv} \end{bmatrix} = \begin{bmatrix} V_{sa1}=V_{sa2} \\ V_{sb1}=V_{sc2} \\ V_{sc1}=V_{se2} \\ V_{sd1}=V_{sb2} \\ V_{se1}=V_{sd2} \end{bmatrix} ; \begin{bmatrix} i_A^{inv} \\ i_B^{inv} \\ i_C^{inv} \\ i_D^{inv} \\ i_E^{inv} \end{bmatrix} = \begin{bmatrix} i_{sa1}+i_{sa2} \\ i_{sb1}+i_{sc2} \\ i_{sc1}+i_{se2} \\ i_{sd1}+i_{sb2} \\ i_{se1}+i_{sd2} \end{bmatrix} \quad (2)$$

where $V_{ABCDE}^{inv}$ and $i_{ABCDE}^{inv}$ are the inverter voltages and currents, $V_{sabcdej}$ and $i_{sabcdej}$ are the two machines' voltages and currents ($j$ =1, 2).

These components are described in $\alpha\beta_1$ and $\alpha\beta_2$ planes by the application of transformation as mentioned earlier:

$$\begin{bmatrix} V_{\alpha1}^{inv} \\ V_{\beta2}^{inv} \\ V_{\alpha2}^{inv} \\ V_{\beta2}^{inv} \\ V_0^{inv} \end{bmatrix} = \begin{bmatrix} V_{s1\alpha1}=V_{s2\alpha2} \\ V_{s1\beta1}=-V_{s2\beta2} \\ V_{s1\alpha2}=V_{s1\alpha1} \\ V_{s1\beta2}=V_{s2\beta1} \\ 0 \end{bmatrix} ; \begin{bmatrix} i_{\alpha1}^{inv} \\ i_{\beta2}^{inv} \\ i_{\alpha2}^{inv} \\ i_{\beta2}^{inv} \\ i_0^{inv} \end{bmatrix} = \begin{bmatrix} i_{s1\alpha1}+i_{s2\alpha2} \\ i_{s1\beta1}-i_{s2\beta2} \\ i_{s1\alpha2}+i_{s1\alpha1} \\ i_{s1\beta2}+i_{s2\beta1} \\ 0 \end{bmatrix} \quad (3)$$

where $V_{\alpha\beta j0}^{inv}$ and $i_{\alpha\beta j0}^{inv}$ are the inverter voltages and currents in $\alpha\beta_1/\alpha\beta_2$ frame. $V_{sj\alpha\beta j}$ and $i_{sj\alpha\beta j}$ are the stator voltages and currents.

Deriving out of (3), the FPIMs have two sets of current components ($\alpha\beta_1$ and $\alpha\beta_2$) and one zero-sequence component. Moreover, since the vector of FPIMs requires only one set of current components, independent control of the two-machine drive is possible due to the additional set of current components provided by the DOF via a proper phase transposition shown in Fig. 1 [17]. This latter aligns the second machine winding with the inverter $\alpha\beta_2$ plane.

The electromagnetic and mechanical equations of the two FPIM in the stationary reference frame are given by [18]:

$$\begin{cases} V_{s1\alpha\beta1}^{inv}=R_{s1}i_{s1\alpha\beta1}+L_{s1}\frac{di_{s1\alpha\beta1}}{dt}+L_{m1}\frac{di_{r1}}{dt}=R_{s2}i_{s2\alpha\beta2}+L_{s2}\frac{di_{s2\alpha\beta2}}{dt} \\ V_{s2\alpha\beta2}^{inv}=R_{s2}i_{s2\alpha\beta2}+L_{s2}\frac{di_{s2\alpha\beta2}}{dt}+L_{m2}\frac{di_{r2}}{dt}=R_{s1}i_{s1\alpha\beta1}+L_{s1}\frac{di_{s1\alpha\beta1}}{dt} \\ 0=R_{rj}i_{rj}+L_{rj}\frac{di_{rj}}{dt}+L_{mj}\frac{di_{sj\alpha\beta j}}{dt}-j\omega\left(L_{mj}i_{sj\alpha\beta j}-L_{rj}i_{rj}\right) \\ T_{emj}=\frac{5p_j}{2}\left(\phi_{sj\alpha j}i_{sj\beta j}-\phi_{sj\beta j}i_{sj\alpha j}\right) \\ J_j\frac{d\omega_{mj}}{dt}=T_{emj}-T_{Lj}-f_j\omega_{mj} \end{cases} \quad (4)$$

where $\phi_{sj\alpha\beta j}$ stator flux linkages, $R_{sj}$ stator resistance, $R_{rj}$ rotor resistance, $L_{sj}$ stator inductance, $L_{m1}$ mutual inductance, $L_{rj}$ rotor inductance, $p_j$ pair poles, $J_j$ moment of inertia, $f_j$ damping coefficient, $T_{emj}$ electromagnetic torque, $T_{Lj}$ the load torque, and $\omega_{mj}$ rotor mechanical speed.

## 3. CONVENTIONAL DIRECT TORQUE CONTROL FOR TWO-MACHINE DRIVE

In this control strategy, the switching sequences, Fig. 2, of the THL-FP inverter are directly applied using a predetermined look-up table. This latter is built on the digital responses of the hysteresis controllers of the error between the reference and actual values of stator flux and the electromagnetic torque and the stator flux position [19].

An additional DOF is introduced in the five-phase system, with appropriate stator windings connections to the inverter terminals, Fig. 1, and the orthogonal relationship between the two $\alpha\beta_1$ and $\alpha\beta_2$ planes, for independent control of two machines [14]. In this case, two independent DTC controllers of above mentioned are used, and following the independence criterion, the look-up table is developed in $\alpha\beta_1$ for the FPIM1 and $\alpha\beta_2$ for the second FPIM, as given in Table 1.

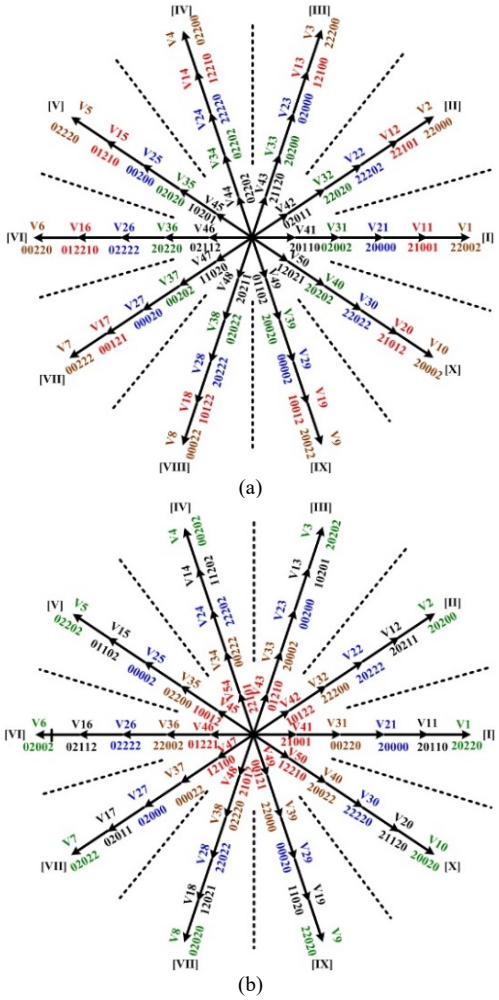


Fig. 2 – The VV and switching states of a three-level five-phase inverter (a) vectors mapped in $\alpha\beta_1$ plan, (b) vectors mapped in $\alpha\beta_2$ plan.

*Table 1*

Switching table for FPIM

| | $\varepsilon_{tem}$ | | | | | | |
|---|---|---|---|---|---|---|---|
| $\varepsilon_{\phi j}$ | 3 | 2 | 1 | 0 | -1 | -2 | -3 |
| 1 | Vi+1 | Vi+21 | Vi+31 | V0 | Vi+39 | Vi+29 | Vi+9 |
| 0 | Vi+4 | Vi+24 | Vi+34 | V0 | Vi+39 | Vi+29 | Vi+9 |

For example, if the stator flux of the FPIM1 lies in sector X and flux needs to decrease $\varepsilon_{\phi s1}$=0 while the electromagnetic torque must be increased $\varepsilon_{Tem1}$=3, the voltage vector (VV) V4 with switching sequence of 02200 in $\alpha\beta_1$ plane will be applied. Moreover, if the position of the stator flux of the second FPIM lies in the sector IV and flux needs to be increased $\varepsilon_{\phi s2}$=1. At the same time, the electromagnetic torque must be decreased $\varepsilon_{Tem2}$=-1, the voltage vector V33 with a switching sequence of 20002 in $\alpha\beta_2$ plane, it will be applied. The naming of the VV is the same in both planes for the simplicity of the look-up tables. The logic selection block applies the two chosen VV for the two machines each for half of the sampling time, *i.e.*, The VV V4 will be applied for the half first sampling time and V33 for the second half. Figure 3 illustrates the structure of

the DTC scheme.

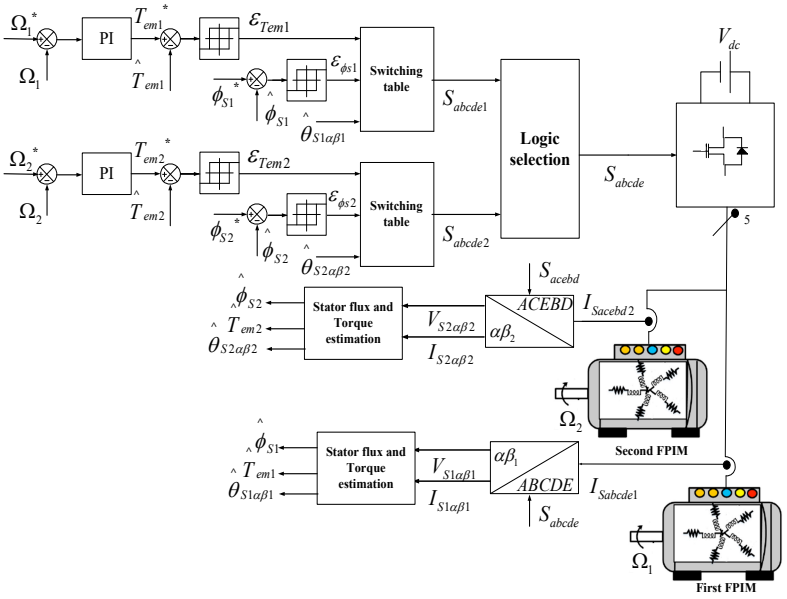


Fig. 3 – Depicts the basics of the $DTC_c$ scheme for the two parallel-connected FPIM framework.

## 4. CMV STATUS

As summarized in Table 2, every switching sequence in the THL-FP inverter is characterized by an output phase voltage that generates specific CMV waveforms as indicated in eq. (5) [15]:

$$U_{cm}=\frac{U_{AZ}+U_{BZ}+U_{CZ}+U_{DZ}+U_{EZ}}{5} \quad (5)$$

where: $U_{AZ}$, $U_{BZ}$, $U_{CZ}$, $U_{DZ}$, and $U_{EZ}$ are the THL-FP inverter phase voltages output concerning the midpoint (Z) of the dc-link. The path of the CMV in two parallel connected FPIM fed by the THL-FP inverter is shown in Fig. 1.

*Table 2*

THL-FP inverter switching sequences

| Switching state | Conducting switches | Phase voltage |
|---|---|---|
| 2 | Upper two | $+V_{dc}/2$ |
| 1 | Middle two | $0V_{dc}$ |
| 0 | Lower two | $-V_{dc}/2$ |

### 4.1 CMV STATUS IN $DTC_C$ SCHEME

In the method mentioned earlier, the CMV status generated by the selected VV is equal to $\pm V_{dc}/2$, *e.g.*, both the switching sequence of the zero VV (ZVV) used in DTC have a phase voltage of $\pm V_{dc}/2$ for each sequence. Thus, according to (5), the produced CMV is equal to $\pm V_{dc}/2$, and similar to the remaining VV. On the grounds of this, the present paper extends the CMV reduction method of TATTE [15] to a parallel connected drive. Table 3 illustrates the peak-to-peak CMV and the theoretical waveforms.

### 4.2 IMPROVED CMV STATUS FOR THE PROPOSED $DTC_{CMV}$

In contempt of the previously mentioned method, the proposed approach employs 31 VV, to synthesis the virtual voltage vectors (VVV), selected for their capability to reduce the CMV to $\pm V_{dc}/10$. The selected VV are 10 large VV (V1-V10) and 10 small VV (V31-V40). As for the medium VV in the TATTE method, the selected vectors are (V11-V20), in addition to a ZVV with a switching sequence of 11111, *i.e.*, the medium VV V20 having switching sequences of 21012 with $+V_{dc}/2$, $0V_{dc}$, $-V_{dc}/2$, $0V_{dc}$, $+V_{dc}/2$ output phase voltage. Thus, from (5), the CMV for this VV is $+V_{dc}/10$, like the remaining VV.

*Table 3*

Peak-to-peak CMV and the theoretical waveforms

| VV | CMV peak [V] | Theoretical waveform of CMV |
|---|---|---|
| V1-V10 | $\pm V_{dc}/10$ | 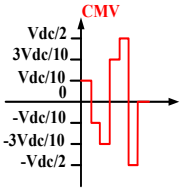 |
| V11-V20 | $\pm V_{dc}/10$ | |
| V21-V20 | $\pm 3V_{dc}/10$ | |
| V31-V40 | $\pm V_{dc}/10$ | |
| V0 | $\pm V_{dc}/2$ | |
| ZVV | 0 | |



## 5. $DTC_{CMV}$ BASED ON CMV REDUCTION APPROACH

In sinusoidal distributed winding multiphase machines, the auxiliary plane, hence the third harmonic component, does not contribute to the developed electromagnetic torque and must be eliminated for better performance, as reported in [20]. However, both planes are essential for the multi-machine drive's operation in the present case and cannot be eliminated since they remain excited.

### 5.1 CONCEPT AND SELECTION OF THE VVV

As mentioned in sections 1 and 3, $\alpha\beta_1$ plane and $\alpha\beta_2$ are utilized to control the FPIM1 and FPIM2, respectively. From the space vector of the THL-FP inverter in Fig. 4 (a), collinear VV in $\alpha\beta_1$ plane, *i.e.* V3, V13, V23, V33, and V43 have a different location and direction in $\alpha\beta_2$ and vis-versa [20]. This peculiarity is exploited in a manner that applied VV results in the cancellation of the either $\alpha\beta_1$ or $\alpha\beta_2$ in the original method. To do so, in the proposed $DTC_{CMV}$, 20 virtual voltage vectors (VVV) are synthesized out of the predefined 31 VV in section IV. So, the large and medium VV herein are classified as large VVV VVLX and the small and medium VV as small VVV VVSX, where X = 1-10. The selection of these VVVs follow the same working principle as in the $DTC_c$ [15]. Figure 4 (b) shows the mapping of this VVV.

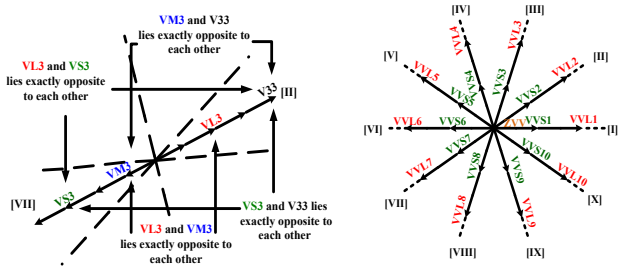


(a) (b)

Fig. 4 – (a) Selection of VVV, (b) VVV mapped in αβ plane.

As in DTC$_c$, the selection of the VVV is made upon a predefined look-up table based on the requirement of the stator flux and electromagnetic torque. It is further explained as follows, if the $\alpha\beta_1$ stator flux of the FPIM1 lies in sector II and both the stator flux and torque needs to be increased, either the VVL4 or the VVS4 will be selected based on the digital output of the five-level torque hysteresis controller. As for the second FPIM, if the $\alpha\beta_2$ stator flux lies in sector X, and flux needs to be decreased, and to increase the torque, then the VVL3 or VVS3 are selected, as illustrated in Table 4.

*Table 4*

VVV look-up table.

| | | Sector | | | | | | | | | |
|---|---|---|---|---|---|---|---|---|---|---|---|
| $\varepsilon_{\phi sj}$ | $\varepsilon_{Temj}$ | I | II | III | IV | V | VI | VII | VIII | IX | X |
| 1 | 2 | VVL3 | VVL4 | VVL5 | VVL6 | VVL7 | VVL8 | VVL9 | VVL10 | VVL1 | VVL2 |
| | 1 | VVS3 | VVS4 | VVS5 | VVS6 | VVS7 | VVS8 | VVS9 | VVS10 | VVS1 | VVS2 |
| | 0 | ZVV | ZVV | ZVV | ZVV | ZVV | ZVV | ZVV | ZVV | ZVV | ZVV |
| | -1 | VVS9 | VVS10 | VVS1 | VVS2 | VVS3 | VVS4 | VVS5 | VVS6 | VVS7 | VVS8 |
| | -2 | VVL9 | VVL10 | VVL1 | VVL2 | VVL3 | VVL4 | VVL5 | VVL6 | VVL7 | VVL8 |
| 0 | 2 | VVL4 | VVL5 | VVL6 | VVL7 | VVL8 | VVL9 | VVL10 | VVL1 | VVL2 | VVL3 |
| | 1 | VVS4 | VVS5 | VVS6 | VVS7 | VVS8 | VVS9 | VVS10 | VVS1 | VVS2 | VVS3 |
| | 0 | ZVV | ZVV | ZVV | ZVV | ZVV | ZVV | ZVV | ZVV | ZVV | ZVV |
| | -1 | VVS8 | VVS9 | VVS10 | VVS1 | VVS2 | VVS3 | VVS4 | VVS5 | VVS6 | VVS7 |
| | -2 | VVL8 | VVL9 | VVL10 | VVL1 | VVL2 | VVL3 | VVL4 | VVL5 | VVL6 | VVL7 |

Where: ZVV=11111

## 5.2 SELECTION OF THE ACTUAL VV

The applied VV are selected according to the output of the VVV table, as illustrated in Table 5.

*Table 5*

Actual VV look-up table.

| Large VVV | VVL1 | VVL2 | VVL3 | VVL4 | VVL5 | VVL6 | VVL7 | VVL8 | VVL9 | VVL10 |
|---|---|---|---|---|---|---|---|---|---|---|
| Location of stator flux of auxiliary plane | IX-III | II-VI | V-IX | VIII-II | I-V | IV-VIII | VII-I | X-IV | VIII-II | I-IV |
| Actual large VV | V1 | V2 | V3 | V4 | V5 | V6 | V7 | V8 | V9 | V10 |
| Location of stator flux of auxiliary plane | IV-VIII | VII-I | X-IV | III-VII | VI-X | IX-III | II-VI | V-IX | VIII-II | I-V |
| Actual medium VV | V11 | V12 | V13 | V14 | V15 | V16 | V17 | V18 | V19 | V20 |
| Small VVV | VVS1 | VVS2 | VVS3 | VVS4 | VVS5 | VVS6 | VVS7 | VVS8 | VVS9 | VVS10 |
| Location of stator flux of auxiliary plane | IX-III | II-VI | V-IX | VIII-II | I-V | IV-VIII | VII-I | X-IV | VIII-II | I-IV |
| Actual small VV | V31 | V32 | V33 | V34 | V35 | V36 | V37 | V38 | V39 | V40 |
| Location of stator flux of auxiliary plane | IV-VIII | VII-I | X-IV | III-VII | VI-X | IX-III | II-VI | V-IX | VIII-II | I-V |
| Actual medium VV | V11 | V12 | V13 | V14 | V15 | V16 | V17 | V18 | V19 | V20 |

For further explanation, if Table 4 selects the VVL4 for FPIM1 and the $\alpha\beta_2$ stator flux of this machine is in sector V the medium VV V14 will be applied for the first half of the sampling frequency. As for the second half, if Table 4 output for the FPIM2 is VVS7 and the $\alpha\beta_1$ stator flux components lie within the first sector, the small VV V37 will be applied for the second half of the sampling period, similarly for the remaining VV.

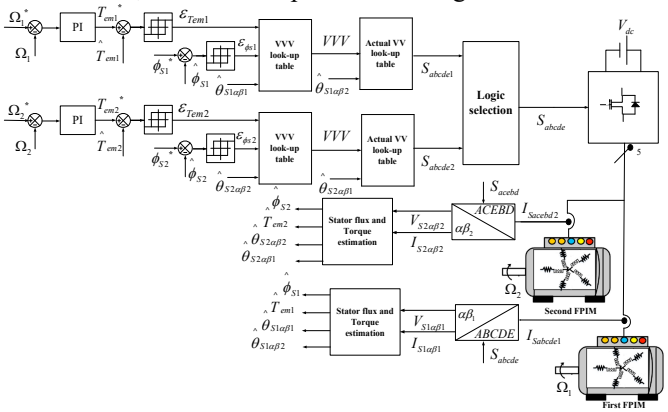


Fig. 5 – Block diagram of DTC$_{CMV}$.

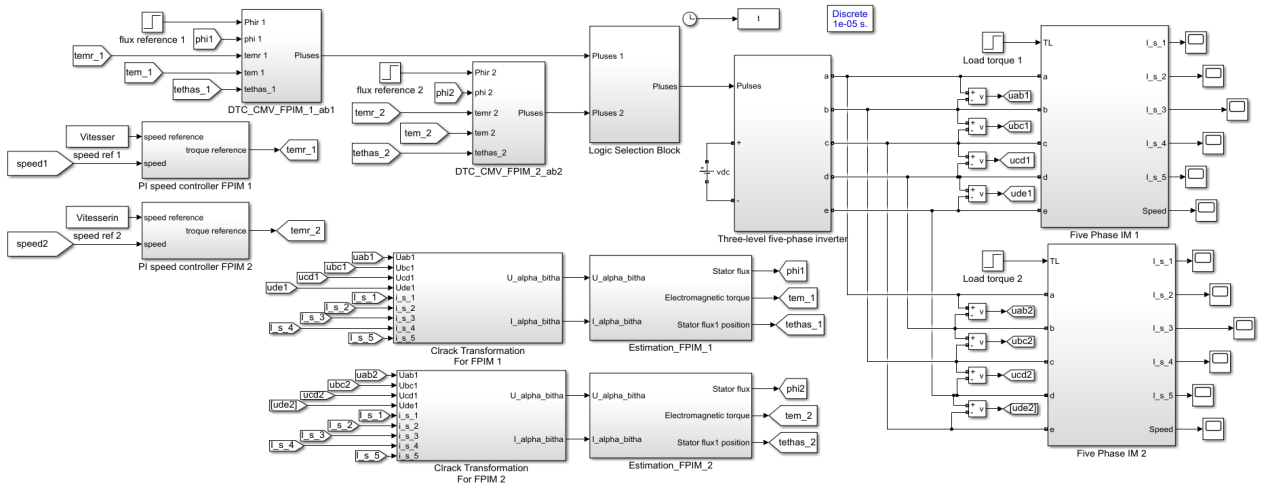


Fig. 6 – Simulation model of $DTC_{CMV}$ in MATLAB/Simulink.

Figure 5 illustrates the block diagram for the proposed $DTC_{CMV}$. A performance evaluation of the proposed $DTC_{CMV}$ is compared to $DTC_C$ MATLAB/Simulink.

Figure 6 shows the implementation of the proposed scheme in Simulink. The machine's parameters are given in Table 6.

*Table 6*

Parameters of FPIM.

| $P_{rated}$ [kw] | $V_{rated}$ [V] | $\omega_{rated}$ [rpm] | $R_s$ [Ω] | $R_r$ [Ω] | $L_s$ [Ω] | $L_r$ [Ω] | $L_m$ [H] | J [Kg.m$^2$] | f $\left[\frac{\text{Nm.s}}{\text{rad}}\right]$ | $T_{em}$ [N.m] | p |
|---|---|---|---|---|---|---|---|---|---|---|---|
| 0.745 | 200 | 1400 | 10 | 6.3 | 0.4642 | 0.4612 | 0.4212 | 0.03 | 0.0001 | 8 | 2 |

## 6. SIMULATION RESULTS

A performance evaluation of the proposed $DTC_{CMV}$ is compared to $DTC_C$ MATLAB/Simulink; Fig. 6 shows the implementation of the proposed scheme in Simulink. The machine's parameters are given in Table 6.

Figures 7-12 summarize the obtained results for the two FPIMs under different testing conditions for both control strategies. In this test, both FPIMs accelerate from a standstill to 100 rad/s and -100 rad/s in 0.5 s. Then at $t$ = 1.5 s, the machines start deaccelerating and reversing at $t$ = 2 s to reach the command values of -100 rad/s and 100 rad/s at $t$ = 2.5 s, respectively, under full load conditions.

Figure 6 (a and b) depicts the rotor speed responses of both FPIMs for the two DTC schemes, showing that both machines follow their reference command successfully. Since the PI speed controller parameters are the same in both cases, both schemes exhibit the same performance.

Figure 7 shows the electromagnetic torque response of the two machines. From the present results, it is observable that the electromagnetic torque of both machines complies with changes in the load torque and rotor speed.

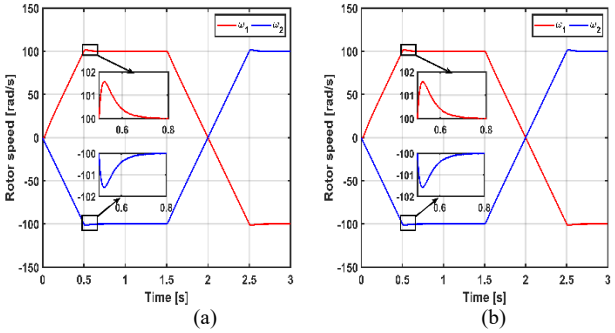


Fig. 7 – Rotor speed response: (a) $DTC_c$, (b) $DTC_{CMV}$.

Furthermore, the $DTC_{CMV}$ has reduced the torque ripples by 39 % compared to $DTC_c$. The stator flux trajectory in $\alpha\beta_1$ and $\alpha\beta_2$ are shown in Figure 9. The $DTC_c$ gives a better and faster response than $DTC_c$, reducing the flux ripples by 22 %.

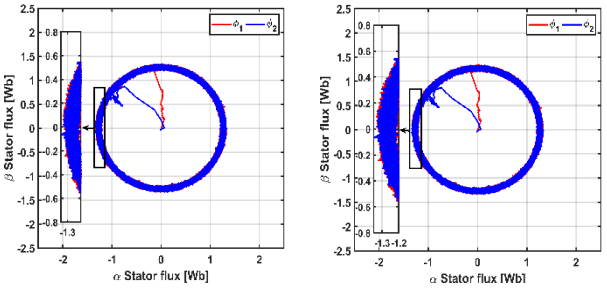


Fig. 9 – Stator flux response: (a) $DTC_c$, (b) $DTC_{CMV}$.

Figure 10 illustrates phase "a" stator current. It can be noticed that the $DTC_c$ has a less distorted current waveform and better current THD by 6% compared to $DTC_{CMV}$.

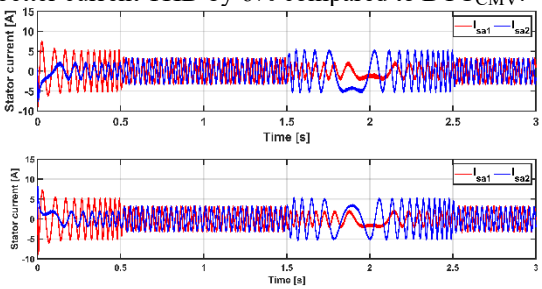


Fig. 10 – Phase "a" stator current waveform: (a) $DTC_c$, (b) $DTC_{CMV}$.

The CMV waveforms generated by both $DTC_{CMV}$ and $DTC_c$ are illustrated in Fig. 11. The CMV peak-to-peak value has been successfully reduced to $\pm V_{dc}/10$ in $DTC_{CMV}$ compared to $DTC_c$ with $\pm V_{dc}/2$, regardless of the different operating conditions.

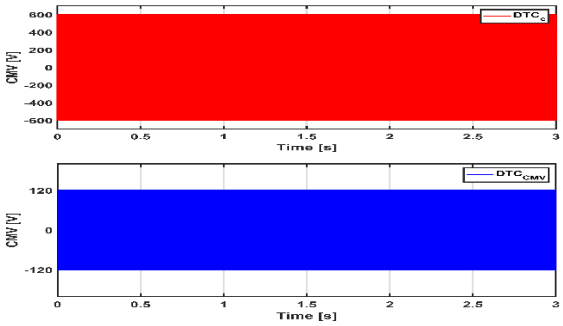


Fig. 11 – CMV waveforms: (a) $DTC_c$, (b) $DTC_{CMV}$.

The simulation results show that the proposed scheme is superior while preserving the driver's independence and decoupling between the stator flux and torque of the two machines regardless of the operation conditions, steady/transient state, and motoring/generating mode.

Table 7 summarizes the simulation results for the two DTC schemes.

*Table 7*

Comparative analysis of the performance of $DTC_c$ and $DTC_{CMV}$

| Performance | Assessment parameters | FPIM1 | | FPIM2 | |
|---|---|---|---|---|---|
| | | $DTC_c$ | $DTC_{CMV}$ | $DTC_c$ | $DTC_{CMV}$ |
| $T_{em}$ | Ripples (Nm) | 2.671 | 2.0848 | 2.384 | 2.1539 |
| $\emptyset_s$ | Ripples (Wb) | 0.156 | 0.1147 | 0.175 | 0.1084 |
| $i_s$ | THD (%) | 22.81 | 28.29 | 18.39 | 21.93 |
| CMV | Peak-to-peak value (V) | 600 | 120 | 600 | 120 |

## 7. CONCLUSIONS

In the THL-FP inverter, the generated CMV is a natural consequence of the switching action damaging the machine's bearing. Thus, this work has proposed an extension of the TATTE method for CMV reduction for DTC of two FPIM connected in parallel fed by THL-FP inverter, preserving the simplicity of the conventional scheme. The proposed method has successfully reduced the CMV to $\pm V_{dc}/10$ peak-to-peak compared to $\pm V_{dc}/2$ in the DTC. This reduction is accomplished by analyzing the CMV pattern of the applied VV. Furthermore, the proposed approach has reduced the flux and torque ripple content by 22 % and 39 %, respectively, compared to the conventional DTC with a trade-off increased current THD by 6 % in the proposed scheme. Modern electrical vehicles can use the extended method to enhance drive reliability and performance.

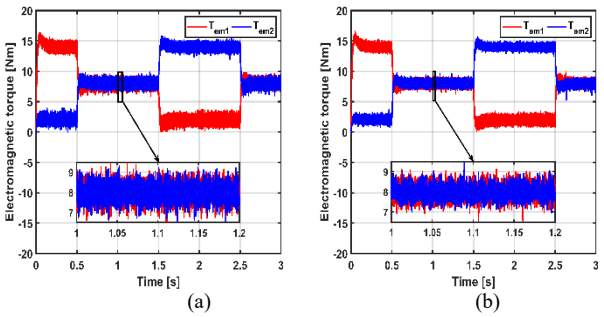


Fig. 8 – Electromagnetic torque response: (a) $DTC_c$, (b) $DTC_{CMV}$.

*Received on 28 August 2023*

## REFERENCES


1. J.C. Li et al., *Design and experimental evaluation of a 12 kW large synchronous reluctance motor and control system for elevator traction,* IEEE Access, **8**, pp. 34256–34264 (2020).
2. S.K. Cho, K.H. Jung, J.Y. Choi, *Design optimization of interior permanent magnet synchronous motor for electric compressors of air-conditioning systems mounted on EVs and HEVs*, IEEE Transactions on Magnetics, **54**, *11*, pp. 1–5 (2018).
3. E. Levi, *Multiphase electric machines for variable-speed applications.* IEEE Transactions on industrial electronics, **55** *5*, pp. 1893–1909, (2008).
4. S. Guedida, B. Tabbache, K. Nounou, M. Benbouzid, *Direct torque control scheme for less harmonic currents and torque ripples for dual star induction motor*, Revue Roumaine des Sciences Techniques—Série Électrotechnique Et Énergétique, **68**, *4*, pp. 331–338 (2023).
5. S.A. Gaikwad, S.M. Shinde, *Review on five-phase induction motor fed by five-phase voltage source inverter with different conduction mode*m International Conference on Industry 4.0 Technology (I4Tech), IEEE (2020).
6. S. Guedida, B. Tabbache, K.M.S. Benzaoui, K. Nounou, M. Nesri, *Novel speed sensorless DTC design for a five-phase induction motor with an intelligent fractional order controller based-MRAS estimator*, Power Electronics and Drives, **9**, *1*, pp. 63–85 (2024).
7. E. Benyoussef, S. Barkat, *Direct torque control based on space vector modulation with balancing strategy of dual star induction motor.* Rev. Roum. Sci. Techn. – Électrotechn. Et Énerg., **67**, *1*, pp.15–20 (2022).
8. K.M.S. Benzaoui, E. Benyoussef, A.Z. Kouache, *Stator flux and speed sensorless control for dtc-ann of two parallel-connected five-phase induction machines based on sliding mode observer*, Majlesi Journal of Electrical Engineering (2024).
9. R. Belal, M. Flitti, M.L. Zegai, *Tuning of PI speed controller in direct torque control of dual star induction motor based on genetic algorithms and neuro-fuzzy schemes*, R Rev. Roum. Sci. Techn. – Électrotechn. Et Énerg., **69**, *1*, pp. 9–14 (2024).
10. E. Benyoussef, S. Barkat, *Three-level direct torque control based on balancing strategy of five-phase induction machine*, Rev. Roum. Sci. Techn. – Électrotechn. Et Énerg., **67**, *2*, pp. 93–98 (2022).
11. E. Robles, et al., *Common-mode voltage mitigation in multiphase electric motor drive systems.* Renewable and Sustainable Energy Reviews, **157**, p. 111971 (2022).
12. E. Robles, et al., *Advanced power inverter topologies and modulation techniques for common-mode voltage elimination in electric motor drive systems.* Renewable and Sustainable Energy Reviews, 2021. **140**, p. 110746 (2021).
13. M. Turzyński, P. Musznicki, *A review of reduction methods of impact of common-mode voltage on electric drives*, Energies, **14**, *13*, p. 4003 (2021).
14. M. Fernandez et al., *New modulation technique to mitigate common mode voltage effects in star-connected five-phase ac drives.* Energies, **13**, *3*, p. 607 (2020).
15. Y.N. Tatte, M.V. Aware, *Direct torque control of five-phase induction motor with common-mode voltage and current harmonics reduction.* IEEE Transactions on Power Electronics, **32**, *11*, pp. 8644–8654 (2016).
16. Y.N. Tatte, M.V. Aware, *Torque ripple and harmonic current reduction in a three-level inverter-fed direct-torque-controlled five-phase induction motor*, IEEE Transactions on Industrial Electronics, **64**, *7*, pp. 5265–5275 (2017).
17. T. Kamel et al., *Extended Kalman filter based sliding mode control of parallel-connected two five-phase PMSM drive system.* Electronics, **7**, *2*, p. 14 (2018).
18. M. Jones, E. Levi, S.N. Vukosavic, *Independent control of two five-phase induction machines connected in parallel to a single inverter supply*, IECON 32nd Annual Conference on IEEE Industrial Electronics (2006).
19. A. Bıçak, A. Gelen, *Sensorless direct torque control based on seven-level torque hysteresis controller for five-phase IPMSM using a sliding-mode observer.* Engineering Science and Technology, International Journal, **24**, *5*, pp. 1134–1143 (2021).
20. Y.N. Tatte et al., *Performance improvement of three-level five-phase inverter-fed DTC-controlled five-phase induction motor during low-speed operation*, IEEE Transactions on Industry Applications, **54**, *3*, pp. 2349–2357 (2018).